

## 6. ANTARCTICA—T. Scambos and S. Stammerjohn

### a. Overview—T. Scambos and S. Stammerjohn Eds.

Last year we reported on an unusual Antarctic climate and sea ice anomaly that developed during late winter-early spring 2016 (Stammerjohn and Scambos 2017; see also Schlosser et al. 2018; Stuecker et al. 2017). This anomaly pattern coincided with record-breaking negative southern annular mode (SAM) index values. Antarctic-wide climate anomalies, including weakened westerly winds, high continental surface pressures and temperatures, and the lowest spring sea ice extent on record, stood in stark contrast not only to the beginning of 2016, but also to the previous four record-breaking high sea ice years (2012–15). This unusual climate anomaly pattern continued until late summer 2017 (February–March), after which SAM index values slowly shifted towards positive for the remainder of the year (except for a short-lived reversal in October). Sea ice extent remained low for most of 2017, as discussed in Section 6e.

In general, 2017 was notable for its strong regional climate anomalies. An anticyclone pattern in January in the South Pacific abruptly shifted to an intense cyclonic anomaly in late summer–autumn (February–May). A strong zonal wave-three pattern then emerged in winter (June–September). Sea ice extent remained below average for the entirety of 2017, with record lows persisting for the first four months, followed by the re-emergence of the Maud Rise polynya in the Weddell Sea in mid-September. The year 2017 was also distinguished by the second smallest Antarctic ozone hole observed since 1988. (Note: throughout the chapter, anomalies and standard deviations are with respect to the 1981–2010 climatological mean, unless otherwise specified.)

Additional highlights for 2017:

- In association with the strong cyclonic pattern in the South Pacific during February–May, anomalously warm near-surface atmosphere conditions persisted over much of West Antarctica, including over the ocean areas from the Ross Sea to the Bellingshausen Sea. Record maximum surface temperatures were observed at several western Peninsula stations in March and on the Ross Ice Shelf in May, along with anomalously warm summer–autumn SSTs,

shallower ocean mixed layers, and delays in the autumn ice edge advance over the West Antarctic ocean sector. The seasonal melt extent and melt index over the continent were the second highest since 2005, mostly due to strong positive anomalies of air temperature over most of the West Antarctic coast. In contrast, the East Antarctic Plateau recorded record low mean temperatures in March. Over the coast and adjacent ocean, conditions were near average.

- In contrast to autumn, winter ushered in anomalously low surface pressures and temperatures over the continent, and a pronounced zonal wave-three pattern existed over midlatitudes from June to September. However, by spring much of the continent experienced near-average pressures and slightly above-average temperatures from October to December, with an East Antarctic station setting a record high temperature in October. Exceptions were a record low continental surface pressure recorded for November on the West Antarctic Ice Sheet and a low-pressure anomaly centered over the northwestern Weddell Sea (~60°S and ~40°W), which contributed to anomalously warm surface conditions over the central-eastern Weddell Sea (~30°W to ~30°E). The latter was coincident with the Maud Rise polynya, which expanded and persisted into early December.
- The brief appearance of the Maud Rise polynya in 2016 and its greater presence in 2017 is significant, as it appears to announce a revival of deep ocean convection in the eastern Weddell Sea (see Sidebar 6.1).

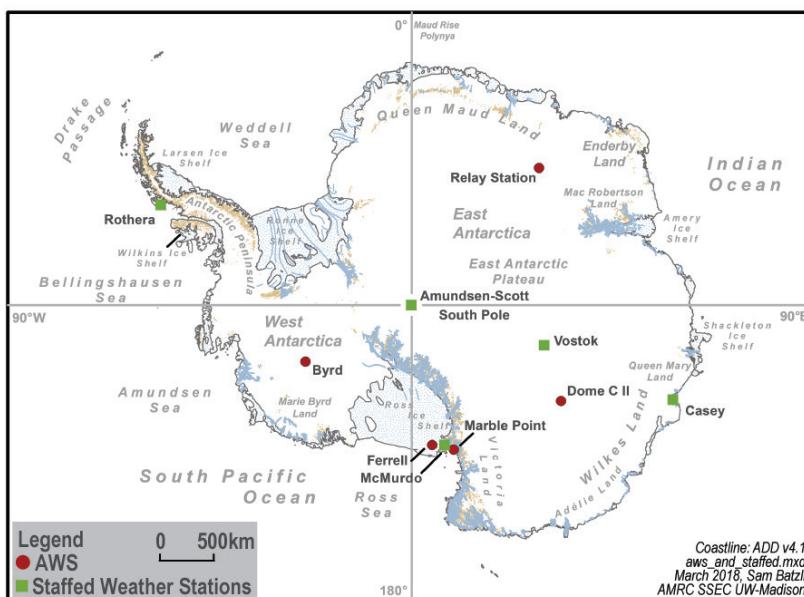


Fig. 6.1. Map of stations and other regions discussed in the chapter.

- The mid-depth Southern Ocean (~500–1500 m) continued to warm at rates up to  $0.02^{\circ}\text{C yr}^{-1}$  while the surface ocean continued to cool by  $-0.015^{\circ}$  to  $-0.05^{\circ}\text{C yr}^{-1}$ , freshen, and acidify.

The state of Antarctica’s climate, weather, ice, ocean, and ozone in 2017 are presented below. Place names used throughout this chapter are provided in Fig. 6.1.

*b. Atmospheric circulation and surface observations—*  
K. R. Clem, S. Barreira, R. L. Fogt, S. Colwell, C. Costanza, L. M. Keller, and M. A. Lazzara.

Atmospheric circulation patterns are the main drivers of all other aspects of this climate summary, affecting sea ice, precipitation, weather records, and even ozone loss. Moreover, long-term changes in climate are impacting ocean circulation (e.g., Schneider et al. 2012) and surface melt patterns (e.g., van den Broeke 2005) and thereby affecting the ice mass balance of the Antarctic ice sheet.

For this detailed analysis of the atmospheric circulation and temperature and pressure anomalies, the European Centre for Medium-Range Weather Forecasts interim reanalysis (ERA-Interim) is utilized as it is shown to be the most reliable representation of Antarctic tropospheric pressure and temperature among all modern global reanalyses (Bracegirdle and Marshall 2012). Figure 6.2 shows the monthly geopotential height (Fig. 6.2a) and temperature (Fig. 6.2b) anomalies averaged over the polar cap ( $60^{\circ}$ – $90^{\circ}\text{S}$ ) and the monthly circumpolar zonal wind (Fig. 6.2c) anomalies averaged over  $50^{\circ}$ – $70^{\circ}\text{S}$ . Anomalies are contoured and the standard deviation level is indicated by colored

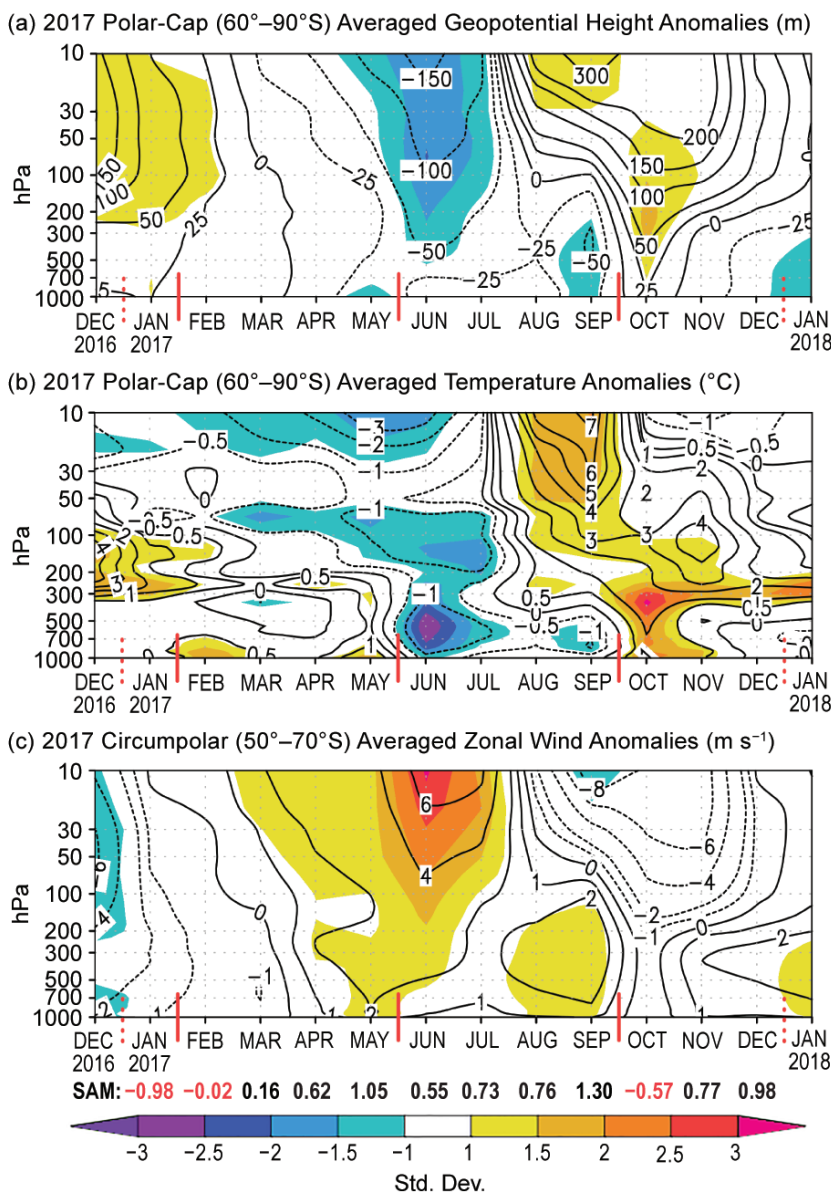


**FIG. 6.2.** Area-averaged (weighted by cosine of latitude) monthly anomalies over the southern polar region in 2017 relative to 1981–2010: (a) polar cap ( $60^{\circ}$ – $90^{\circ}\text{S}$ ) averaged geopotential height anomalies (contour interval is 50 m up to  $\pm 200$  m with additional contour at  $\pm 25$  m, and 100 m contour interval after  $\pm 200$  m); (b) polar cap averaged temperature anomalies (contour interval is  $1^{\circ}\text{C}$  with additional contour at  $\pm 0.5^{\circ}\text{C}$ ); (c) circumpolar ( $50^{\circ}$ – $70^{\circ}\text{S}$ ) averaged zonal wind anomalies (contour interval is  $2 \text{ m s}^{-1}$  with additional contour at  $\pm 1 \text{ m s}^{-1}$ ). Shading depicts std. dev. of monthly anomalies from the 1981–2010 climatological average as indicated by color bar at bottom. (Source: ERA-Interim reanalysis.) Red vertical bars indicate the four climate periods used for compositing in Fig. 6.3; the dashed lines near Dec 2016 and Dec 2017 indicate circulation anomalies wrapping around the calendar year. Values from the NOAA CPC Antarctic Oscillation index (herein referred to as the SAM index) are shown below (c) in black (positive values) and red (negative values).

shading. The year was grouped into four periods characterized by relatively consistent climatic fea-

tures: January, February–May, June–September, and October–December. These periods are indicated by vertical red bars at the bottom of each panel in Fig. 6.2. Anomalies for the four groups from their respective group climatological mean are shown in Fig. 6.3, with surface pressure anomalies shown on the left and 2-m temperature anomalies shown on the right. Monthly temperature and pressure anomalies during 2017 are also displayed in Fig. 6.4 for three staffed stations (Amundsen–Scott, Casey, and Rothera) and three automatic weather stations (AWS; Byrd, Dome C II, and Ferrell) to examine the monthly variability and extreme events for the surface conditions across the continent.

January 2017 was distinct from the rest of the year with positive pressure anomalies over the continent and primarily negative pressure anomalies between 40° and 60°S (Fig. 6.3a) and slightly weaker-than-average circumpolar westerlies throughout the troposphere and lower stratosphere (Fig. 6.2c). The January circulation pattern is consistent with the negative phase of the southern annular mode (SAM) which continued from late 2016 [the SAM index from NOAA’s Climate Prediction Center (CPC) in January was  $-0.98$ ], and it marks the transition of the late 2016 circulation to opposite sign anomalies in autumn 2017. At the surface, a strong high pressure anomaly was present over the South Pacific poleward to the Amundsen Sea, which through altered temperature advection and sea ice conditions produced negative temperature anomalies of  $\sim 1^\circ\text{C}$  across the Antarctic Peninsula (Figs. 6.3a,b). These features weakened after January, and from February through May they were replaced by an anomalously deep Amundsen Sea Low centered over the northwest Amundsen Sea into the South Pacific (Fig. 6.3c; 6–9 hPa and 2–3 standard deviations below average). The anomalous cyclonic circulation, in conjunction with an anticyclone anomaly in the northwest Weddell Sea, produced well-above-average temperatures across much of West Antarctica during late summer and autumn spanning the western Antarctic Peninsula, Amundsen Sea Embayment, Marie Byrd Land, and Ross Ice Shelf (Fig. 6.3d;  $2^\circ$ – $5^\circ\text{C}$  and  $>3$  standard deviations above average). Temperatures at the Byrd AWS in central West Antarctica were  $2^\circ$ – $5^\circ\text{C}$  above average during February–May, and record maximum monthly mean temperatures were observed on the Antarctic Peninsula in March at both Marambio ( $-2^\circ\text{C}$ ) and Rothera ( $1.2^\circ\text{C}$ ; Fig. 6.4c); Dome C II AWS, on the East Antarctic plateau, reported record low monthly mean temperatures in March ( $-57.1^\circ\text{C}$ , Fig. 6.4e), nearly  $5^\circ\text{C}$  below average.

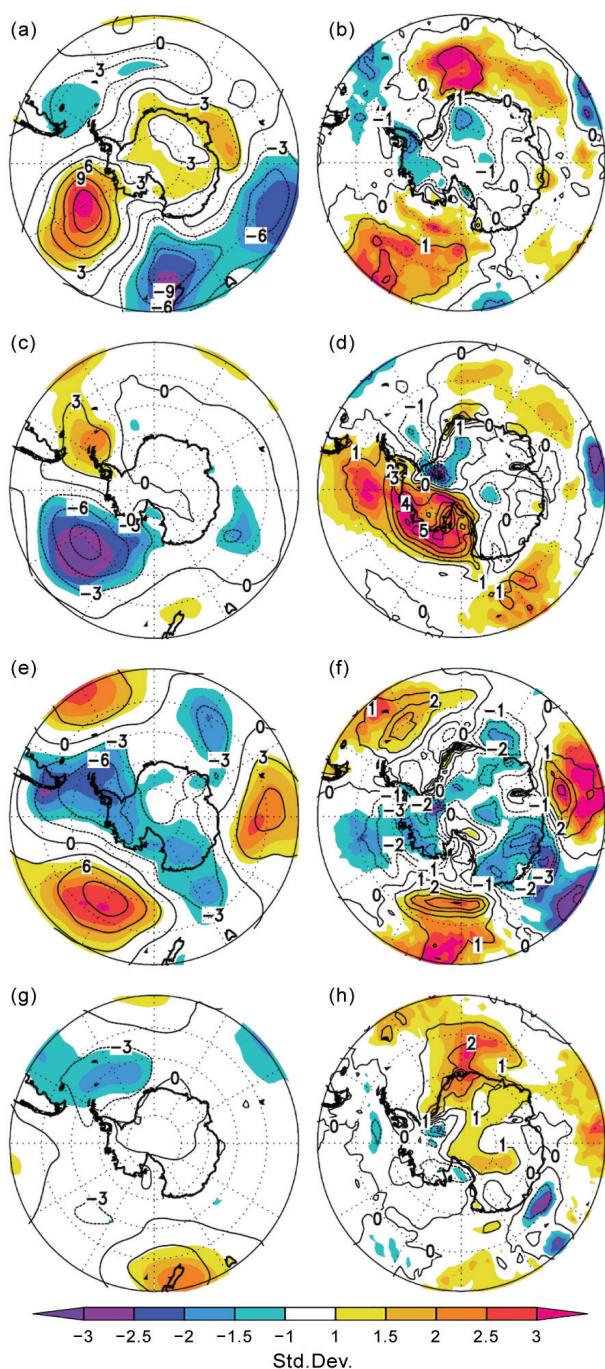


**FIG. 6.3.** (left) Surface pressure anomalies and (right) 2-m temperature anomalies relative to each group’s 1981–2010 climatological average for (a) and (b) Jan 2017; (c) and (d) Feb–May 2017; (e) and (f) Jun–Sep 2017; and (g) and (h) Oct–Dec 2017. Contour interval for surface pressure anomalies is 3 hPa and  $1^\circ\text{C}$  for 2-m temperature anomalies. Shading depicts std. dev. of anomalies relative to the 1981–2010 average of each group. (Source: ERA-Interim reanalysis.)

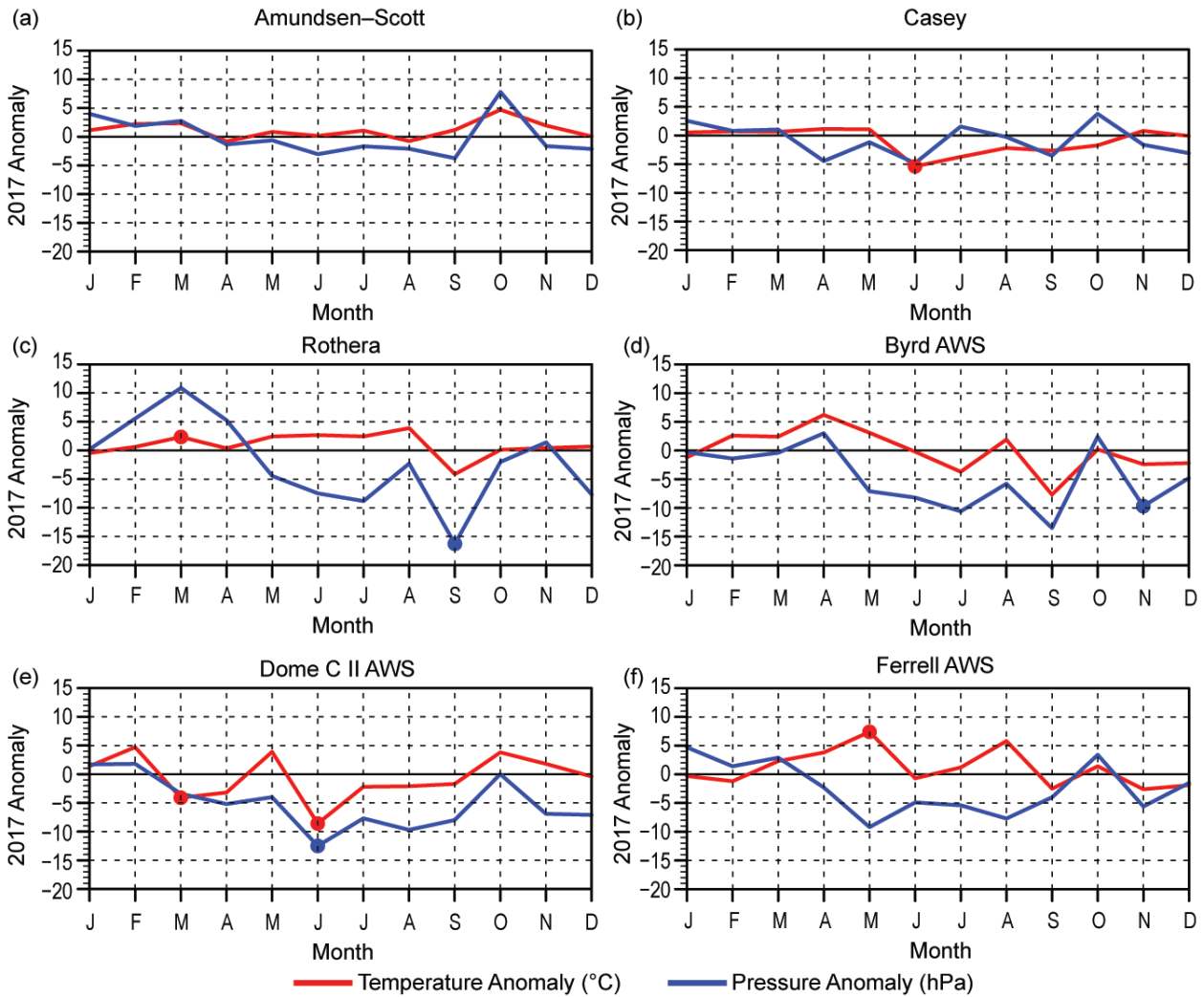


**FIG. 6.4. Monthly Antarctic climate anomalies during 2017 at six representative stations [three staffed (a)–(c), and three automatic (d)–(f)]. Anomalies for temperature (°C) are shown in red and MSLP/surface pressure (hPa) in blue are shown, with filled circles denoting record anomalies for a given month at each station in 2017. All anomalies are based on differences from the monthly 1981–2010 averages. Observational data start in 1957 for Amundsen–Scott, 1959 for Casey, 1976 for Rothera, 1980 for Byrd AWS, and 1981 Dome C II and Ferrell AWS.**

During April (not shown), negative pressure anomalies developed over Wilkes Land and Queen Maud Land, and the associated northerly flow was an important contributor to the late advance of sea ice in the western Ross and eastern Weddell Seas; these cyclonic circulation anomalies were part of a larger shift in the Antarctic circulation as captured to some extent in the polar-cap-averaged geopotential height (Fig. 6.2a) and circumpolar zonal wind anomalies (Fig. 6.2c), both of which changed sign in April and intensified in May. At Casey Station, located in Wilkes Land in coastal East Antarctica, pressure anomalies were the lowest in April, consistent with this circulation shift. On the eastern side of this low pressure system, the northerly flow increased temperatures

across the Ross Ice Shelf, and Ferrell AWS reported a record monthly mean maximum temperature for May of  $-23.1^{\circ}\text{C}$ ,  $7.4^{\circ}\text{C}$  warmer than the climatological average (Fig. 6.4f).

During the winter months (June–September), a pronounced zonal wave-three pattern developed, characterized by three anomalous ridges along  $50^{\circ}\text{S}$  centered at  $90^{\circ}\text{E}$ ,  $150^{\circ}\text{W}$ , and  $30^{\circ}\text{W}$  and a deep low pressure anomaly over the Antarctic Peninsula (Fig. 6.3e). Temperatures were generally below average across the continent, especially on the eastern side of the midlatitude ridges/western side of the troughs, where southerly flow produced cool conditions. Colder-than-average winter temperatures were also observed throughout the troposphere and

stratosphere, accompanied by negative geopotential height anomalies and stronger-than-average circum-polar westerlies in winter (Fig. 6.2); the stratospheric vortex exhibited the greatest positive anomalies of 4–6 m s<sup>-1</sup> above average during June. East Antarctica experienced its most negative temperature anomalies during 2017 in June (2°–6°C below average), with Casey (Fig. 6.4b) and Dome C II AWS (Fig. 6.4e) both setting record low monthly mean temperatures in June (–19.4°C and –57.1°C, respectively). West Antarctica saw its strongest cold anomalies during July (2°–4°C below average) and September (4°–8°C below average; see Byrd AWS temperature anomalies in Fig. 6.4d). The colder-than-average temperatures in September were partially due to the low pressure anomaly over the Antarctic Peninsula, reflected in the record negative monthly mean pressure of 971.3 hPa at Rothera (Fig 6.4c), more than 16 hPa below the climatological average.

A positive temperature/geopotential height anomaly developed in the stratosphere during September and propagated downward into the lower troposphere during October (Fig. 6.2). Positive pressure and temperature anomalies developed at the surface across much of the continent in October, reflected in the observations at Amundsen Scott in Fig. 6.4a; the strongest positive surface air temperature anomalies during October (not shown) were over interior portions of East Antarctica along the Transantarctic Mountains reaching 2°–4°C (> 3 standard deviations) above average, and Vostok Station in the central East Antarctic plateau set a record high monthly mean temperature in October of –51.1°C, 1.7°C higher than the previous record set in 2015. Averaged over the October–December period (Figs. 6.3g,h), the strongest positive temperature anomalies were over Queen Maud Land, while the rest of the continent experienced near-average to slightly-above-average temperatures and near-average pressure to close out 2017; exceptions include the Ross Ice Shelf where below-average temperatures were observed during November due to enhanced southerly flow from the development of an anomalous cyclone in the South Pacific that was consistent with the late austral spring La Niña conditions (see Section 4b) and a record monthly mean low surface pressure value at the Byrd AWS in November (787.7 hPa).

There were several record high monthly-mean wind speeds recorded at various AWS during the year. Ferrell had record high wind speeds in May (9.7 m s<sup>-1</sup>), July (9.5 m s<sup>-1</sup>), and August (10.6 m s<sup>-1</sup>) and Marble Point had a record high wind speed in March (5.7 m s<sup>-1</sup>). Byrd had a record high wind speed in May

(10.6 m s<sup>-1</sup>), and Dome C II had a record in October (5.4 m s<sup>-1</sup>). Relay Station tied its record low wind speed in November (5.5 m s<sup>-1</sup>). The record high wind speeds reflect the incidence of lower than normal pressure for much of the year (Figs. 6.3, 6.4).

#### c. Net precipitation ( $P-E$ )—D. H. Bromwich and S.-H. Wang

Precipitation minus evaporation/sublimation ( $P-E$ ) closely approximates the surface mass balance over Antarctica (e.g., Bromwich et al. 2011; Lenaerts and van den Broeke 2012), except for near-coastal areas where wind-driven transport of snow and meltwater runoff can become significant factors. Precipitation variability is the dominant term for  $P-E$  changes at regional and larger scales over the Antarctic continent. Precipitation and evaporation fields from the Japanese 55-year reanalysis (JRA-55; Kobayashi et al. 2015) were examined to assess Antarctic net precipitation ( $P-E$ ) behavior for 2017. JRA-55, the second generation of JRA, has incorporated many improvements compared to its predecessor JRA-25 (Onogi et al. 2007; Bromwich et al. 2007). The JRA-55 is used here because of these improvements and its low latency, rather than ERA-Interim used elsewhere. Because of the highly uneven distribution of  $P-E$  characteristics (from large Peninsula and coastal West Antarctica values >1000 mm yr<sup>-1</sup> to very low values <50 mm yr<sup>-1</sup> in the high interior), only annual  $P-E$  changes are shown in Fig. 6.5.

Figure 6.5 shows the JRA-55 2017 and 2016 annual anomalies of  $P-E$  (Figs. 6.5a,b) and mean sea level pressure (MSLP; Figs. 6.5c,d) departures from the 1981–2010 average. In general, annual  $P-E$  anomalies over the high interior of the continent were small (within  $\pm 50$  mm yr<sup>-1</sup>), and larger anomalies were observed along the coast, consistent with the low and high net precipitation accumulation in these regions. From JRA-55, the 2016 positive anomalies located along the coast between Queen Maud Land and Mac Robertson Land (between 5°W and 60°E) became weak negative anomalies in 2017, most pronounced near 60°E. The weak negative anomalies over the American Highland (between 70° and 90°E) in 2016 became strongly positive in 2017. Both Queen Mary Land and Wilkes Land (between 90° and 125°E) remained strongly negative. The strong positive anomalies over Adélie Land and Victoria Land (between 125° and 175°E) became near-zero in 2017. The positive anomaly over the eastern Ross Ice Shelf in 2016 evolved into a larger positive anomaly that extended into interior Antarctica in 2017. The largest positive anomalies that were located over the Bellingshausen Sea and the southern Antarctic

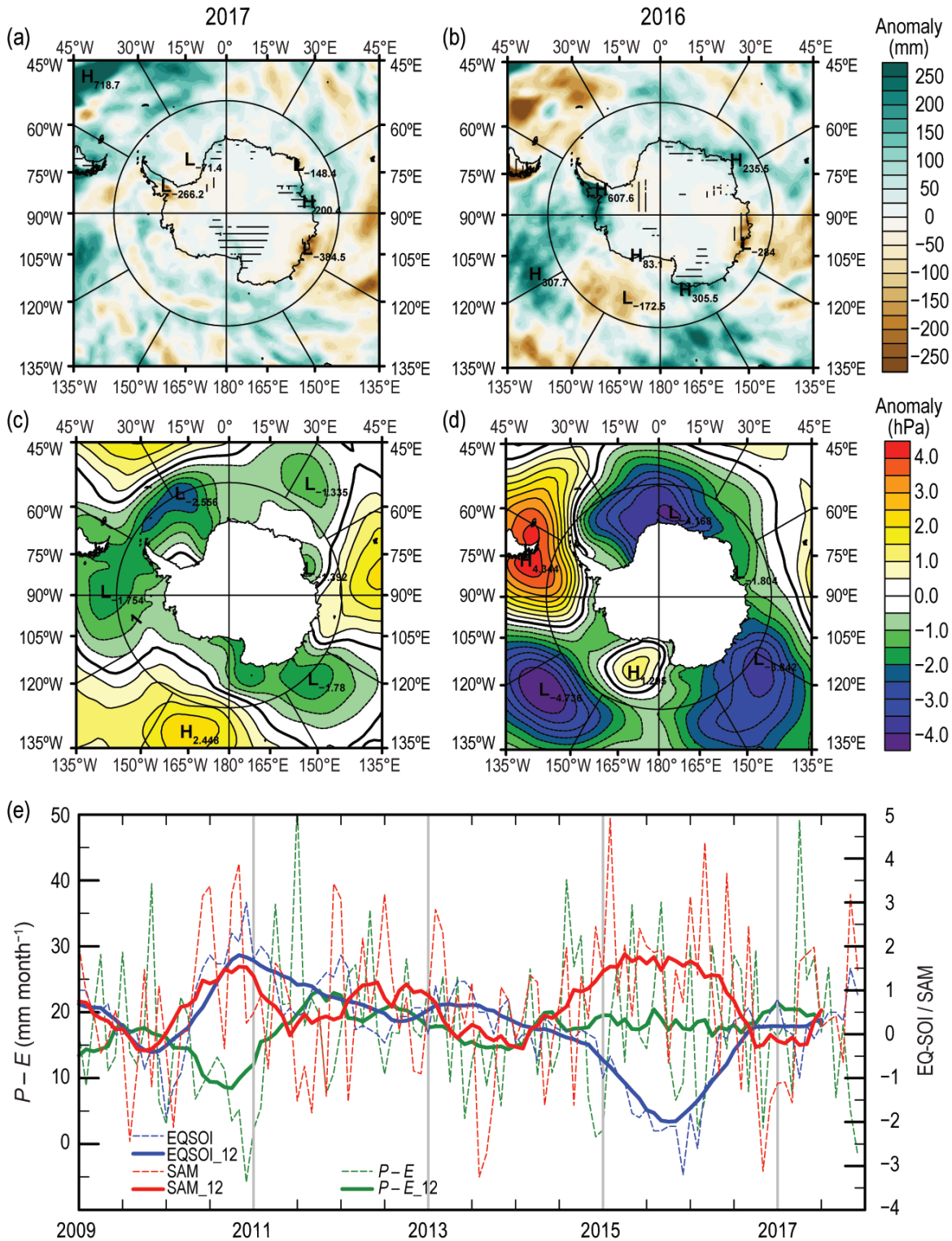


**FIG. 6.5.** (a–d) Annual precipitation minus evaporation ( $P-E$ ) and MSLP anomalies: (a) 2017  $P-E$  anomaly (mm); (b) 2016  $P-E$  anomaly (mm). Antarctic regions with  $> \pm 30\%$  departure from the reference mean are hatched; vertical denotes negative anomaly and horizontal is positive. (c) 2017 MSLP anomaly (hPa); and (d) 2016 MSLP anomaly (hPa). All anomalies are calculated with respect to the 1981–2010 means. (e) Monthly total  $P-E$  (mm; dashed green) for part of West Antarctica bounded by  $75^{\circ}$ – $90^{\circ}$ S,  $120^{\circ}$ W– $180^{\circ}$ , along with index trends for EQ-SOI (dashed blue, from NOAA CPC) and SAM (dashed red, from Marshall 2003). Centered annual running means are plotted as solid lines.

Peninsula (between 110° and 70°W) in 2016 became the second largest negative anomalies in 2017. Similar to 2016, the two sides of the Antarctic Peninsula had opposite anomalies but with a reversal of signs in 2017: positive in the east, negative to the west. The Ronne Ice Shelf anomalies remained negative but were weaker during 2017.

These annual  $P-E$  anomaly features are generally consistent with the mean annual atmospheric circulation implied by the MSLP anomalies (Figs. 6.5c,d). In 2017 (Fig. 6.5c), the MSLP annual anomalies surrounding Antarctica were less regionalized and were weaker than in 2016 (Fig. 6.5d) with strong seasonal variation during 2017 (e.g., Fig. 6.3). The largest positive anomaly center in 2016 over the Drake Passage (~75°W) became the largest negative anomaly in 2017 and extended into the Weddell Sea as the seasons progressed through the year, with a peak in September–November (SON; e.g., Figs. 6.3 e,g). The observed negative anomaly centers over the South Pacific (160°~110°W) and Indian Ocean (105°~165°E) strengthened in the first half of 2017 (e.g., Figs. 6.3a,c). Both anomalies expanded and changed to positive values that covered nearly two-thirds of the Southern Ocean (between 15°E and 90°W) later in the year (SON; e.g., Fig. 6.3e). These seasonal MSLP changes resulted in negative–positive–negative anomaly centers along the East Antarctic coast in the Southern Ocean (Figs. 6.3e, 6.5c). Two secondary negative MSLP anomaly centers located over coastal Ross Sea (between 165°E and 160°W) and the Amery Ice Shelf (~65°E) produced stronger onshore wind flows and resulted in greater than 30% higher  $P-E$  in the interior of the Antarctic continent (Fig. 6.5a). By contrast, two negative  $P-E$  anomalies (~120°E and ~80°W; Fig. 6.5a) were associated with strong offshore flow in 2017 (Fig. 6.5c).

Earlier studies (e.g., Cullather et al. 1998) show that almost half of the moisture transport into interior Antarctica occurs in the West Antarctic sector. Antarctic moisture transport has large interannual variability, often associated with variations of ENSO (e.g., Bromwich et al. 2004) and the southern annular mode (SAM; e.g., Fogt et al. 2011). Figure 6.5e shows the time series, with 12-month running means, of monthly total  $P-E$  over Marie Byrd Land–Ross Ice Shelf (75°–90°S, 120°W–180°) and the monthly equatorial Southern Oscillation index (EQ-SOI) and SAM indices. The NOAA CPC EQ-SOI is a standardized sea level pressure difference centered on the equator between the east Pacific (5°N–5°S, 80°–130°W) and Indonesia (the west Pacific; 5°N–5°S, 90°–140°E) and is negative during warm events. In comparison to

the conventional station-based SOI, EQ-SOI is less susceptible to weather noise and better captures the equatorial trade wind events (see [www.climate.gov/news-features/blogs/enso/why-are-there-so-many-enso-indexes-instead-just-one](http://www.climate.gov/news-features/blogs/enso/why-are-there-so-many-enso-indexes-instead-just-one)).

The EQ-SOI and SAM were in phase (same sign) but have opposite behavior to  $P-E$  in most months from 2010 to mid-2011 (Fig. 6.5e). From then on, EQ-SOI and SAM were out of phase (opposite sign) through early 2016. Both EQ-SOI and SAM were offsetting factors modulating precipitation, resulting in little overall change of  $P-E$ . From late 2016 to early 2017, the MSLP anomalies over the Ross Sea shifted from positive (December–February) to negative (March–May; e.g., Figs. 6.3a,c). A combination of a weak La Niña pattern and a negative SAM resulted in higher  $P-E$  amounts in this region during early 2017. As the seasons progressed into late 2017, both ENSO and SAM indices strengthened and became in phase with each other.  $P-E$  began to show signs of a large decrease in late 2017.

#### d. Seasonal melt extent and duration—L. Wang and H. Liu

Surface melt contributes to accelerated iceberg calving, hence the retreat of ice margins and continental ice mass loss (Scambos et al. 2013; Rignot et al. 2004). The intensity, duration, and spatial extent of surface melt (Tedesco et al. 2013) contribute directly to the enlargement of ice crevasses (Scambos et al. 2000), accelerated glacier ice flow (Zwally et al. 2002), and disintegration of buttressing ice tongues and ice shelves (van den Broeke 2005; Massom et al. 2018).

Surface melt on the Antarctic continent during the 2016/17 austral summer season was estimated from daily passive microwave brightness temperature data at the 19 GHz frequency acquired by the Special Sensor Microwave Imager/Sounder (SSM/IS) onboard the Defense Meteorological Satellite Program (DMSP) F17 satellite in the ascending passes. The data were preprocessed and provided by the U.S. National Snow and Ice Data Center (NSIDC) at level-3 EASE-Grid format (Armstrong et al. 1994) and were analyzed using a wavelet transform-based edge detection method (Ho, Liu et al. 2005). The algorithm delineates each melt event in the time series by tracking its onset and end dates, with the onset day of the first melt event being the start day of the melt season (Fig. 6.6a) and the end day of the last melt event being the end day of the melt season (Fig. 6.6b). The melt duration is then the total number of melting days per pixel during the defined melt season (excluding any refreezing events that may have occurred during this period; Fig. 6.6c). The melt extent and melt index are metrics useful for

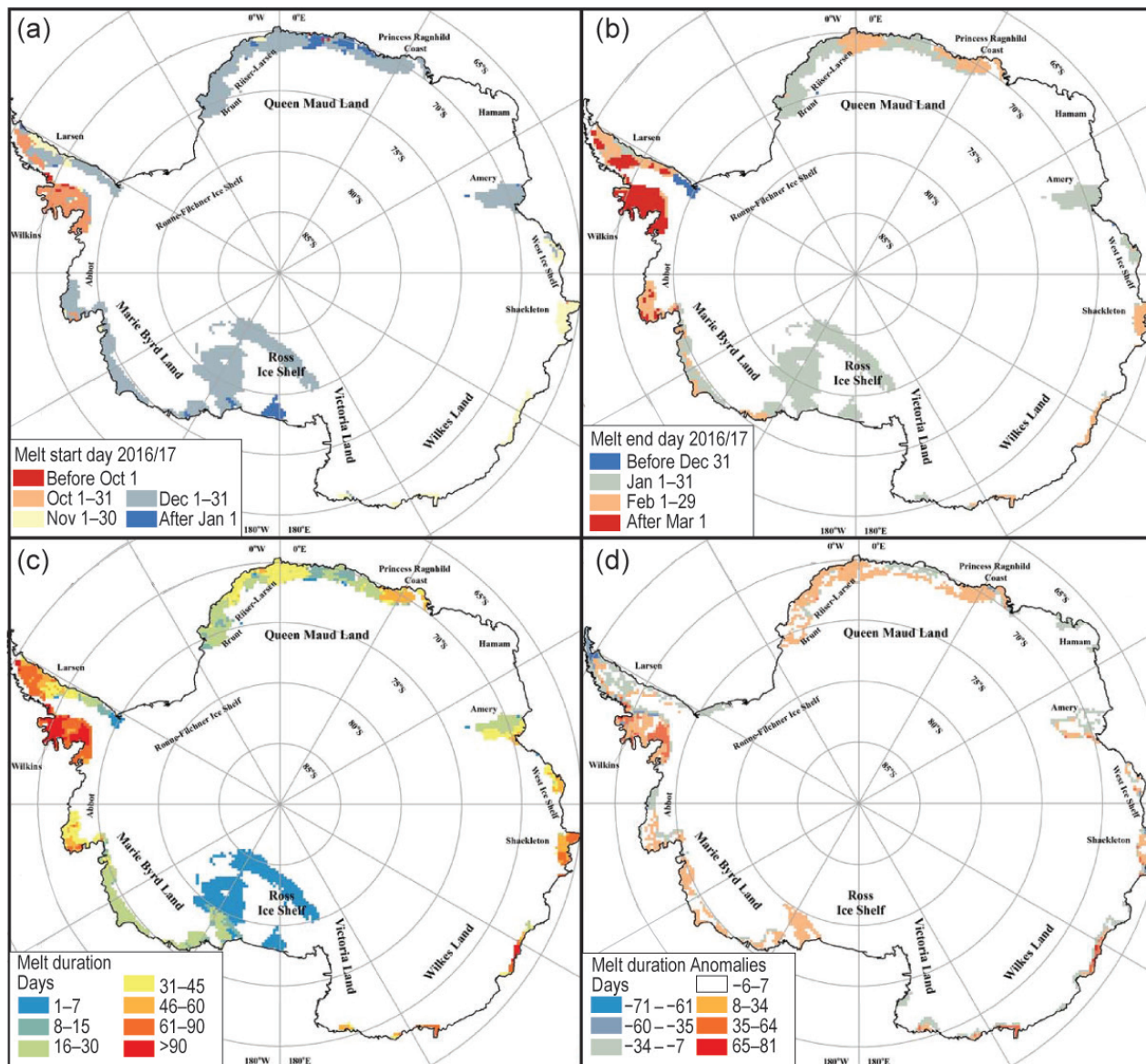


**FIG. 6.6.** Estimated surface melt for the 2016/17 austral summer: (a) melt start day, (b) melt end day, (c) melt duration (days), and (d) melt duration anomalies (days).

quantifying the interannual variability in surface melt (Zwally and Fiegles 1994; Liu et al. 2006). Melt extent ( $\text{km}^2$ ) is the total area that experienced surface melt for at least one day during the melt season. Melt index ( $\text{day} \cdot \text{km}^2$ ) is the sum of the duration (days) of the melt pixels in the study area that describes the strength of melt as the accumulative melt days in a year. The anomaly map (Fig. 6.6d) was created by referencing to the mean melt duration computed over the 1981–2010 period (see also Fig. 3 in Liu et al. 2006).

Figure 6.6a shows that the earliest melt events occurred on the Wilkins Ice Shelf during the austral summer of 2016/17. The early melt area also extended to the tip of the Antarctic Peninsula. Some late but short melt events occurred on the Ross Ice Shelf. The

melt events on the Wilkins Ice Shelf extended to late March 2017 (Fig. 6.6b). Figure 6.6c shows the melt duration in the austral summer of 2016/17 (Fig. 6.6c). Areas with intensive melt (> 45 day duration in orange–red) were the Larsen, Wilkins, and Shackleton ice shelves, and some coastal areas of Wilkes Land and Queen Maud Land. The Shackleton Ice Shelf had an abnormal prolonged melt season this year, which could have been related to the higher-than-average temperature in November and record-breaking low monthly mean pressure recorded at the nearby Casey Station (Keller et al. 2017). Areas with moderate intensity of melt (16–45 day duration in green–yellow) included coastal Queen Maud Land and the Amery Ice Shelf; short-term melt (< 16 day duration in blues)

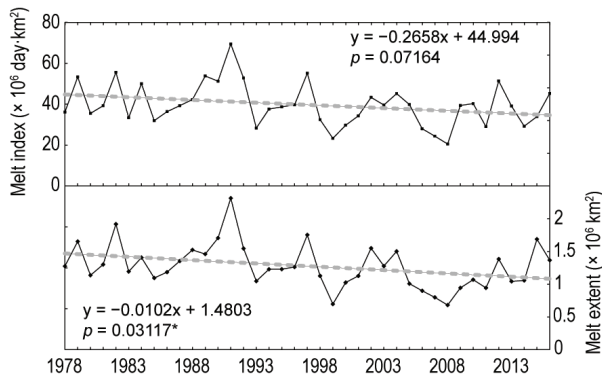


**FIG. 6.7. (a) Melt index ( $\times 10^6$  day $\cdot$ km $^2$ ) from 1978/79 to 2016/17, showing a negative trend (265 800 day $\cdot$ km $^2$  yr $^{-1}$ , not significant at 95%). (b) Melt extent ( $\times 10^6$  km $^2$ ) from 1978/79 to 2016/17, showing a negative trend (10 200 km $^2$  yr $^{-1}$ ,  $p < 0.05\%$ ). The year on the x-axis corresponds to the start of the austral summer melt season, that is, 2008 corresponds to summer 2008/09.**

occurred on the Ross Ice Shelf and small portions of coastal Queen Maud Land. Almost half of the Ross Ice Shelf experienced melt, albeit briefly, in the summer of 2016/17. Compared to the previous year, melt on the Ross Ice Shelf was less extensive. Overall, the 2016/17 melt season was slightly longer than the historical average (Fig. 6.6d), indicating an above-average melt year for Antarctica.

Figure 6.7a shows a non-significant ( $p > 0.05$ ) negative trend (265 800 day $\cdot$ km $^2$  yr $^{-1}$ ) in melt index since 1978, highlighted by the record low melt season observed during austral summer 2008/09. The trend lines were fit using a linear regression between the melt indices and year number. Before adding 2017 to the regression, the negative trend in melt index was significant ( $p < 0.05$ ; Wang and Liu 2017). The marked increase in melt index for 2017 was due to the intensive melt ( $> 90$  days) on the Wilkins Ice Shelf. The negative trend of the melt extent, however, remained significant ( $p < 0.05$ ; Fig. 6.7b), because half of the Ross Ice Shelf did not melt (Fig. 6.6c) as it did in 2016, which reduced the 2017 melt extent as compared to 2016 (Fig. 6.7b). Nonetheless, both the melt extent and melt index were the second highest since 2005. The negative trends are consistent with previous reports (Liu et al. 2006; Tedesco 2009; Tedesco et al. 2009).

**e. Sea ice extent, concentration, and seasonality—**  
P. Reid, S. Stammerjohn, R. A. Massom, J. L. Lieser, S. Barreira, and T. Scambos

Antarctic sea ice performs important roles in the climate system through the formation of dense oxygen rich Antarctic Bottom Water (Johnson 2008) and modulating fluxes across the ocean/atmosphere

interface within the high southern latitudes (Bourassa et al. 2013). It also acts as a buffer for ice shelves against ocean processes (Williams and Squire 2007; Massom et al. 2018).

Net sea ice extent (SIE; the area enclosed by the ice edge consisting of a range in sea ice concentration) and sea ice area (SIA; the actual area covered by sea ice) were well below the 1981–2010 average for all of 2017 (Fig. 6.8b). Following the record low seasonal sea ice cover in November and December 2016 (Reid et al. 2017; Stuecker et al. 2017; Turner et al. 2017; Schlosser et al. 2018), the first four months of 2017 also had record low net SIE, followed by sporadic periods of record low SIE into September. Overall, 130 days of record low SIE occurred during 2017, with 57 individual days of record low SIA between January and early October. The month of February 2017 recorded the lowest monthly mean SIE on record (Schlosser et al. 2018). Other records in 2017 included the lowest observed daily value of SIE in the continuous satellite record (since 1978) on 1 March 2017 of  $2.1 \times 10^6$  km $^2$  (not shown; previous lowest was  $2.3 \times 10^6$  km $^2$  on 27 February 1997). The annual daily maximum was also later than previously observed, on 9 October (previous latest maximum was 3 October 1988). Record low sea ice cover during 2016/17 is in contrast to the long-term (1979–2016) positive trend in net SIE (Turner and Comiso 2017), as discussed further below.

Regionally, early 2017 (January through mid-April) sea ice coverage followed on from the predominantly low net sea ice coverage in late 2016. However, high concentrations of sea ice were observed along much of the coast of East Antarctica ( $\sim 80^\circ$ – $160^\circ$ E) and in parts of the Weddell Sea ( $\sim 30^\circ$ – $60^\circ$ W), for example (Fig. 6.8c). Synoptically, in late 2016 and January 2017, winds around East Antarctica and the Weddell Sea were anomalously easterly, causing an initial southward compaction of the sea ice via Ekman transport while largely retaining the sea ice extent in these regions during the summer season (Figs. 6.8a,c). Consequently, sea ice advanced early across much of East Antarctica. Elsewhere around the coast in early 2017, sea ice coverage was either non-existent or well below average (e.g., Fig. 6.8c). Ocean SSTs around Antarctica through early 2017 were anomalously high (e.g., Fig. 6.8c; Section 6f) and coincident with regions of suppressed ice formation, particularly in the Ross, Bellingshausen, and Amundsen Seas and the eastern Weddell Sea. The suppressed ice formation led to considerably later ice edge advance in these regions, by as much as 50 days later in most of the Amundsen

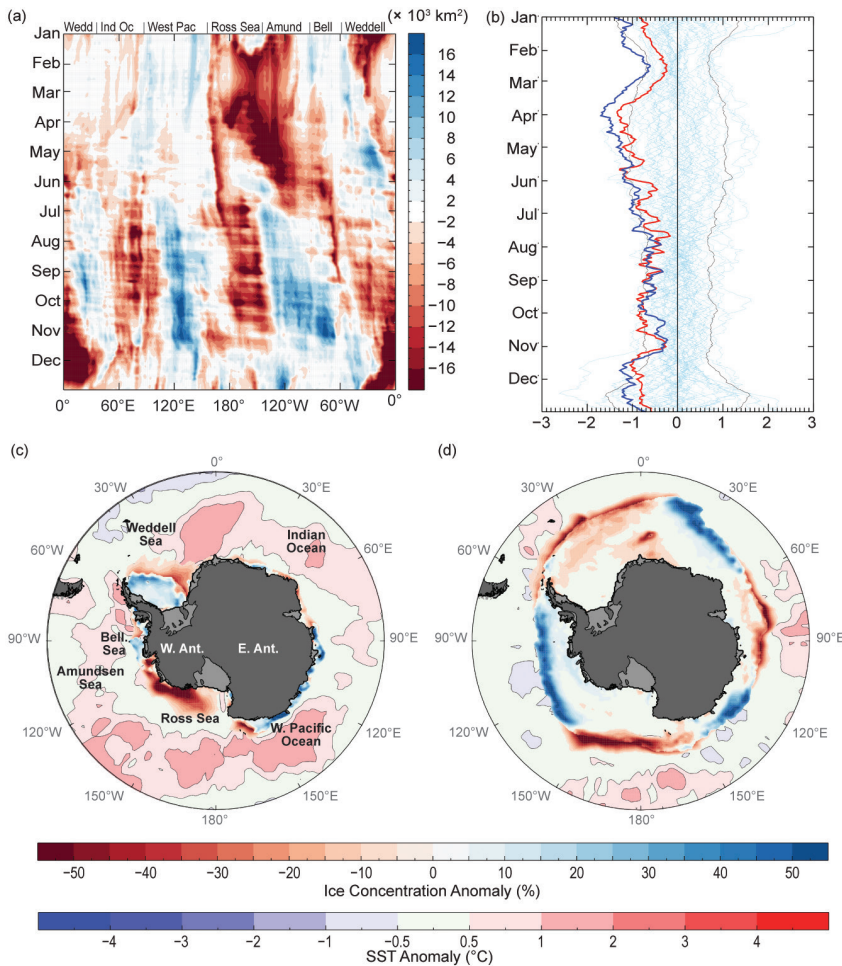


**FIG. 6.8.** (a) Hovmöller plot of daily SH sea ice extent anomalies for 2017 ( $\times 10^3$  km<sup>2</sup> per degree of longitude; from the 1981–2010 mean); (b) net sea ice extent anomaly (blue) and sea ice area anomaly (red) (from 1981–2010 mean); thin blue lines represent the historical daily values of extent for 1979–2015, while the thin black lines represents  $\pm 2$  std. dev. of extent. (c) and (d) sea ice concentration anomaly (%) and SST anomaly ( $^{\circ}$ C; Reynolds et al. 2002; Smith et al. 2008) for (c) Feb. and (d) Sep. 2017. Based on satellite passive-microwave ice concentration data [Cavalieri et al. 1996, updated yearly, for climatology; and Maslanik and Stroeve (1999) for the 2017 sea ice concentrations].

Sea, as reflected in the negative duration anomaly in this region (Fig. 6.9a).

The atmospheric circulation pattern changed during April with deep low pressure systems developing north of the Weddell Sea ( $\sim 30^{\circ}$ W), Wilkes Land ( $\sim 125^{\circ}$ E), and well north of the Amundsen Sea ( $\sim 100^{\circ}$ W; see Section 6b). This pattern enhanced ice coverage predominantly within the western Weddell Sea while continuing to suppress extent in the Bellingshausen, Amundsen, and Ross Seas through warm air advection and higher-than-normal SSTs. A zonal wave-two atmospheric pattern developed in May (not shown), with synoptic lows centered in the eastern Ross Sea ( $\sim 140^{\circ}$ W) and north of the Amery Ice Shelf

( $\sim 70^{\circ}$ E), promoting sea ice advance (albeit later than normal) in the Ross ( $\sim 120^{\circ}$ W– $180^{\circ}$ ) and Weddell ( $\sim 10^{\circ}$ – $30^{\circ}$ W) Seas. Through May and into early June, SIE continued to be above average across much of East Antarctica but below average in the western Ross, Amundsen, and Bellingshausen Seas and across the eastern Weddell Sea and Indian Ocean sectors ( $\sim 10^{\circ}$ W– $80^{\circ}$ E).

During mid-June, a stationary wave-three atmospheric pattern began to develop (Section 6b), with broad low-pressure centers to the north of the Bellingshausen Sea ( $\sim 80^{\circ}$ W), East Antarctica ( $\sim 140^{\circ}$ E), and Dronning Maud Land ( $\sim 40^{\circ}$ E) that broadly correspond to the SIE anomalies (Fig. 6.8a). This pattern increased southerly cold air outflow in the eastern Ross Sea, far eastern Weddell Sea, and north of Wilkes Land ( $\sim 120^{\circ}$ E), increasing ice coverage and contributing to a positive anomaly in SIE in these regions (Fig. 6.8a). Conversely, intervening warm air advection and higher SSTs associated with this zonal wave-three pattern were observed in the western Weddell and Ross Seas and to the north of the Amery Ice Shelf ( $\sim 60^{\circ}$ – $100^{\circ}$ E), suppressing ice expansion and producing

a negative SIE anomaly (Fig. 6.8a). Interestingly, while the atmospheric zonal wave-three pattern subsided during September, the zonal wave-three pattern within both the patterns of SIE and SST anomalies persisted through early November (Figs. 6.8a,d). It was during this period (September onwards; e.g., Fig. 6.8d) that, again similar to 2016 (Mazloff et al. 2017; Reid et al. 2017), the Maud Rise polynya opened up (see Sidebar 6.1).

Early November saw another change in the circumpolar atmospheric circulation pattern, with the development of a deep Amundsen Sea low pressure system and an associated zonal wave-three pattern. The change in atmospheric circulation influenced

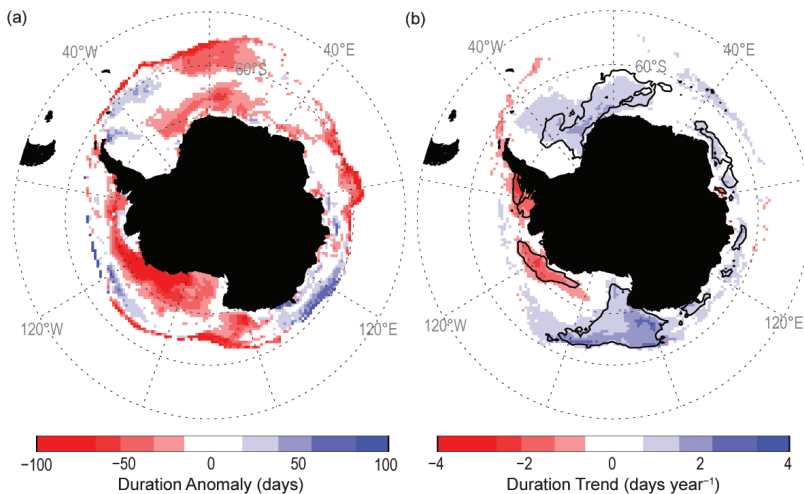


**FIG. 6.9.** Maps showing (a) duration anomaly for the 2016/17 sea ice season in days and (b) duration trend for 1979/80–2016/17 in days yr<sup>-1</sup>. The black contour in (b) delineates those trends with significance at the  $p < 0.01$  significance level.

the regional rate of ice retreat, particularly in the Bellingshausen–Amundsen (60°–120°W) and Weddell (30°W–30°E) Seas where slower and faster retreat occurred, respectively (Fig. 6.8a).

These austral springtime sea ice distribution changes are consistent with the influence of the relatively weak La Niña developing within the tropical Pacific in early November 2017 (see Section 4b), which changed the position of the higher-latitude southern jet streams and hence the cyclonicity around the Antarctic continental edge (Yuan 2004; Stammerjohn et al. 2008). Thus, SIE towards the end of the year and within the Weddell Sea was, in some areas, more than six standard deviations below average. Elsewhere, SIE was close to average, although small pockets of greater-than-average SIE existed within the Amundsen Sea and western Pacific sector (~110°–150°E) associated with wind-driven compaction of the sea ice cover and lower-than-normal SSTs near these regions.

The long-term trend for Antarctic sea ice is regionally and seasonally variable: increased SIE and longer seasonal duration within the Ross and Weddell Seas, and decreased SIE and shorter duration in the Bellingshausen–Amundsen Seas (e.g., Fig. 6.9b for sea ice duration trends over 1979/80–2016/17; see Comiso et al. 2017 for sea ice extent trends). For SIE these changes are largest during January–May (Hobbs et al. 2016). Apart from some areas of the Amundsen Sea, the regional pattern of sea ice coverage during 2017, described above, was in contrast to this long-term trend (Fig. 6.9a), particularly in much of the Ross

Sea and the Weddell Sea through the end of March.

*f. Southern Ocean*—S. Swart, K. Johnson, M. R. Mazloff, A. Meijers, M. P. Meredith, L. Newman, and J.-B. Sallée

In the climate system, the Southern Ocean is disproportionately important when it comes to its storage of heat and carbon. Modification of the upper Southern Ocean could have significant implications for the rate and magnitude of air–sea fluxes (of heat and carbon) and for the ventilation of the ocean interior, thereby altering the effects of climate warming on the ocean system as a whole. Here, we evaluate the state of the Southern Ocean in 2017 by first assessing the upper ocean as the interface between the atmosphere and ocean interior.

We then discuss the changes in intermediate to deep water masses, which are critical pathways to moving heat and carbon to the ocean interior where it will (in general) remain for decades to centuries. Lastly, we report on the status of ocean acidification in the Southern Ocean using newly available biogeochemical observations.

#### 1) UPPER OCEAN

By utilizing all available 2017 hydrographic profiles (40 816 from Argo floats and 11 916 from tagged seals), anomalies of mixed layer depth (MLD) and mixed layer (ML) temperature and salinity (Figs. 6.10a–c) were computed from the climatological (2000–2010) seasonal cycle (see Pellichero et al. 2017). During 2017, the most significant observation is the shallower MLDs (negative anomalies) occurring in the Pacific sector, particularly within the Antarctic Circumpolar Current (ACC), where MLDs are more than 100 m shallower than the climatology. Meanwhile, the Atlantic and Indian sectors are characterized by mixed MLD anomalies.

In contrast to anomalies reported for 2015 and 2016 (Sallée et al. 2016; Mazloff et al. 2017), a markedly warmer ML (Fig. 6.10b) was observed throughout most of the Southern Ocean in 2017, except for the northern subantarctic region of the Atlantic sector. In further contrast, positive Southern Ocean ML temperature anomalies in 2015 were juxtaposed against negative anomalies to the north, indicating a north–south dipole separated by the ACC (Sallée et al. 2016), while in

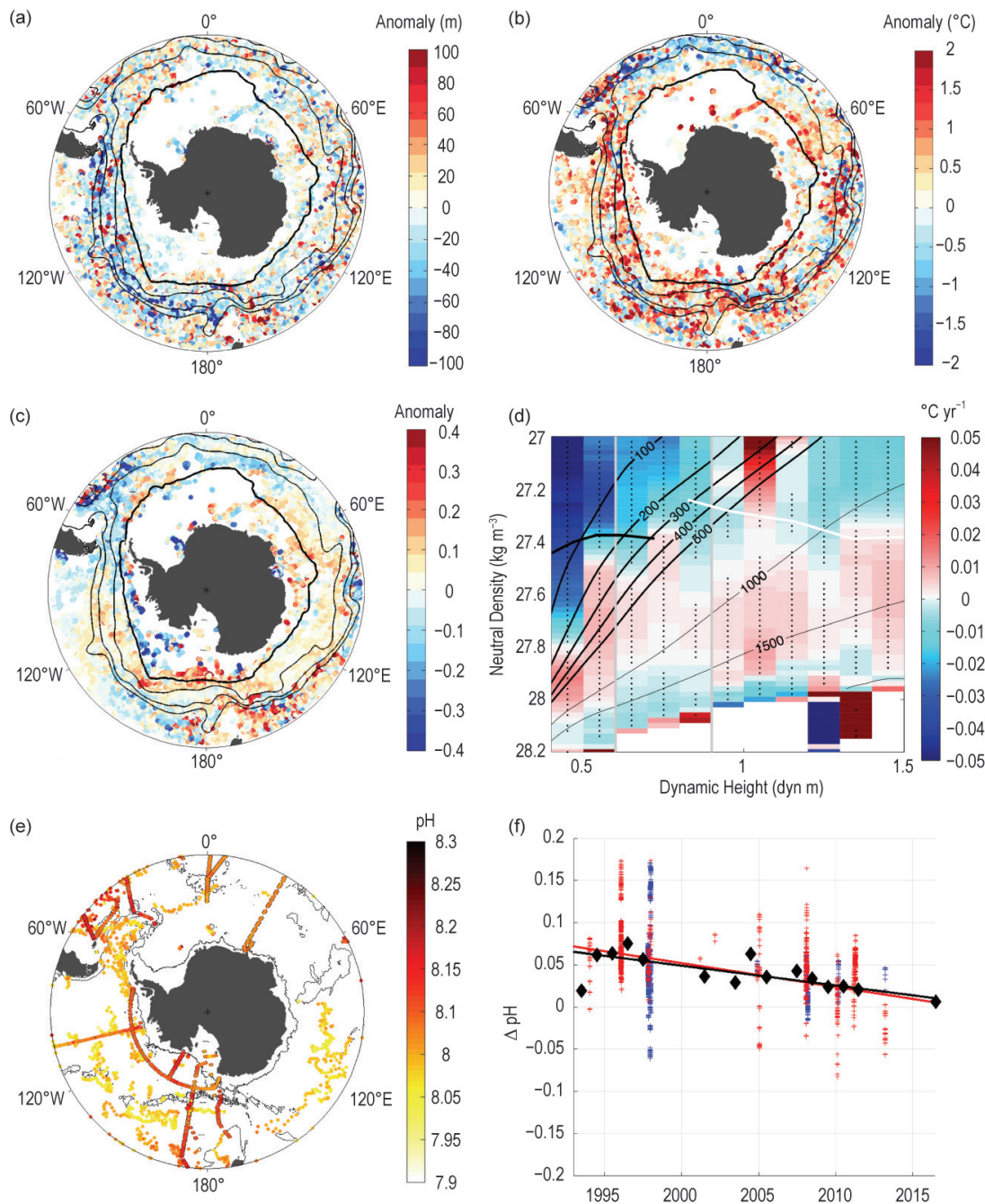


**FIG. 6.10.** (a) Mixed layer depth anomaly (m) in 2017 from the climatological seasonal cycle. The thin black contours represent the main ACC fronts from north to south: northern Subantarctic Front (SAF), main SAF, Polar Front (PF). The thick black contour is the Sep. climatological sea ice extent. (b) Same as (a) but for mixed layer temperature ( $^{\circ}\text{C}$ ). (c) Same as (a) but for mixed layer absolute salinity. (d) Circumpolar average trend in potential temperature (in  $^{\circ}\text{C yr}^{-1}$ ) from Argo float data (seasonal cycle removed), oriented along constant dynamic height and isopycnal surfaces. The thick solid black contour is the T-min layer and the white contour is the S-min layer. Constant pressure surfaces are indicated. Vertical lines indicate the position of the PF (left) and SAF (right). Dots indicate trends in potential temperature significant at the 95% level. (e) Observed upper 30-m pH (black outlined colored dots) from the GLODAPv2 database (Key et al. 2015) spanning 1992–2013 and the SOCCOM pH observations in 2017 (colored dots without outlines). The 3000-m bathymetry contour is shown in black. (f) Changes in pH via two different methods: black diamonds are annual averaged GLODAPv2 comparisons (1992–2013) to all SOCCOM float data (2014–17), while red/blue pluses denote the discrete GLODAPv2 comparisons to only 2017 float data and all other float data, respectively (based on criteria explained in the text). The black and red lines are the linear fit to the respective color markers.

2016, ML temperature anomalies defined a quadrupole delimited by ocean basins (Mazloff et al. 2017).

In 2017 warmer ML temperatures north of the mean September ice edge (thick black contour in Figs. 6.10a-c) generally coincided with shallower MLDs (negative anomalies; Fig. 6.10a) and increased ocean stratification (not shown). However, deeper MLDs (positive anomalies) appearing in the Indian sector of the Southern Ocean (centered on 60°E near the mean September ice edge) coincided with anomalously saline mixed layers (Fig. 6.10c) and reduced ocean stratification (not shown). South of the ACC (and mean September ice edge) there are fewer observations, but overall the data suggest a negative MLD anomaly (shallower) in the West Antarctic sector together with strongly negative ML salinity (fresher) and positive (higher) ML temperature anomalies. These fresher MLs may be linked with a long-term increase in wind-driven transport of freshwater northward (Haumann et al. 2016) and/or increased sea ice melt in summer (February) 2017 (Section 6e). From the Maud Rise region (~3°E) towards East Antarctica positive ML salinity anomalies (Fig. 6.10c) were observed, which resulted in weak stratification. These changes may be linked to the anomalously low sea ice conditions experienced in the eastern Weddell Sea (Section 6e) together with the recent re-emergence of the Maud Rise polynya and its associated impacts on the upper ocean via enhanced air-sea exchanges and ventilation of warmer, saltier interior water masses (see Sidebar 6.1).

## 2) INTERMEDIATE OCEAN

Significant thermohaline changes are occurring below the surface layers of the Southern Ocean. Due to the slow time scales of these changes (unlike the more temporally sensitive surface mixed layer properties just described), it is more appropriate to discuss multi-year changes (2002–16). The gravest empirical mode (GEM; see methods in Meijers et al. 2011; Swart et al. 2010), a highly effective method to reconstruct subsurface property fields from sea surface height, is used to map thermal changes at intermediate depths (thermocline depth to 2000 m). The GEM uses a current inventory of all Argo float profiles (2002 to 2016) to derive circumpolar-averaged potential temperature trends approximately oriented along stream-following dynamic height contours, here shown on constant isopycnal surfaces (Fig. 6.10d). Such a coordinate choice removes aliasing and trends due to frontal movements and vertical heave.

Overall, there was a consistent warming of up to  $0.02^{\circ}\text{C yr}^{-1}$  (Fig. 6.10d) and salinification (not shown:

$27.6\text{--}28\text{ kg m}^{-3}$ ) of the densest Antarctic Intermediate Water (AAIW) and Circumpolar Deep Water (CDW) throughout the Southern Ocean over 2002–16. This may be related to changes in westerly winds (due to long-term increases in the SAM; Böning et al. 2008). Lying above these depths, two fairly distinct negative trends were observed, one north of the Polar Front ( $> 0.8\text{ dyn m}$ ), which indicates cooling of the upper AAIW and Subantarctic Mode Water (SAMW;  $-0.01^{\circ}\text{C yr}^{-1}$ ), and the other south of the Polar Front, which indicates relatively strong cooling and freshening of winter and surface water (e.g., Haumann et al. 2016) ranging from  $-0.015^{\circ}$  to  $-0.05^{\circ}\text{C yr}^{-1}$ . The cooling of SAMW in the northern ACC does not contradict the general warming trend observed beyond the northern ACC, as this may be related to increased volume and hence heat content of SAMW and AAIW predominantly caused by wind-driven changes, namely increased wind stress curl (Gao et al. 2018).

## 3) BIOGEOCHEMICAL STATUS: CONTINUED OCEAN ACIDIFICATION

The new Southern Ocean Carbon and Climate Observations and Modeling project (SOCCOM) array currently has 105 active profiling floats, allowing a characterization of ocean pH variability at shorter time scales and higher spatial resolution. Ocean pH is decreasing as anthropogenic  $\text{CO}_2$  enters the ocean and forms carbonic acid (causing ocean acidification). Ocean acidification challenges the viability of organisms producing  $\text{CaCO}_3$  shells and has fundamental impacts on the ocean carbon cycle.

Observed pH in the upper 30 m from the GLODAPv2 database (1992–2013 observations as black outlined colored dots in Fig. 6.10e; Key et al. 2015; Olsen et al. 2016) is compared to SOCCOM pH observations in 2017 (colored dots without black outlines). It is qualitatively apparent that the GLODAPv2 estimates have higher pH. Two methods were used to quantify these differences. For the first method, all upper 150-m GLODAPv2 observations from 1992 to 2013 were used, and float observations (from 2014 to 2017) that were within 20-km and 5-m depth of the GLODAPv2 observations were identified. Differences in pH between GLODAPv2 and float observations were determined and bin-averaged for each year of GLODAPv2 observations (black diamonds in Fig. 6.10f); any year with less than five matches was eliminated. (The additional data point for 2016 shows the mean offset between float pH and hydrocast pH, the latter acquired during float deployments; Johnson et al. 2017). A second method identified all

## SIDEBAR 6.1: RETURN OF THE MAUD RISE POLYNYA: CLIMATE

**LITMUS OR SEA ICE ANOMALY?**—S. SWART, E. C. CAMPBELL, C. H. HEUZÉ, K. JOHNSON, J. L. LIESER, R. MASSOM, M. MAZLOFF, M. MEREDITH, P. REID, J.-B. SALLÉE, AND S. STAMMERJOHN

The Maud Rise polynya is a persistent area of open water within the sea ice cover of the Southern Ocean, which overlies an area of elevated topography called Maud Rise (66°S, 3°E) located in the eastern sector of the Weddell Sea (Fig. SB6.1a). It is termed a “Weddell polynya” if it grows and migrates westward into the central Weddell Sea. This larger sized polynya was first observed in satellite data in 1974 and recurred for each of the two subsequent austral winters (Zwally and Gloersen 1977; Carsey 1980). Its large size, ~300 000 km<sup>2</sup>, meant that it could contribute strongly to the transfer of heat from the ocean to the atmosphere in winter and, hence, instigate dense water production and the renewal of deep ocean waters in the Weddell Sea (Gordon 1978). The amount of deep water formed via this route was estimated at 1–3 Sverdrups (Martinson et al. 1981). The 1974–76 polynya may have been responsible for up to 34% of observed warming of the deep Southern Ocean (Zanowski et al. 2015). Smaller features, perhaps associated with topographically driven upwelling of warm waters, have been observed subsequently (Comiso and Gordon 1987), but a large polynya had not re-appeared until recently and unexpectedly during austral winters 2016 and 2017.

Following the Maud Rise polynya development in 2016 (Mazloff et al. 2017), mid-September 2017 saw the opening of a longer lived and larger polynya over the same region. The 2017 polynya grew quickly but its size remained quite static at approximately 50 000 km<sup>2</sup> until 3 November, after which it more than tripled in size over a period of a week. The sudden expansion is possibly the result of a considerable change in atmospheric circulation due to the development of a La Niña in early November (Section 6e), combined with an anomalously earlier spring ice edge retreat (see Section 6e). The polynya continued to expand over the following month (Fig. SB6.1b) and reached its maximum size of 295 000 km<sup>2</sup> (larger than New Zealand) on 2 December 2017 before coalescing with the open ocean. Overall, it contributed to a significantly large negative anomaly in sea ice concentration (see Section 6e).

Two under-ice biogeochemical profiling floats from the Southern Ocean Carbon and Climate Observations and Modeling (SOCCOM) project were present at Maud Rise before, during, and after the 2016 and 2017 polynyas. Both floats surfaced and transmitted data within the 2017 polynya (Fig. SB6.1b). These data show the appearance of cold and fresh subsurface anomalies in late 2016 (extending from ~100 to 300 m depth in Figs. SB6.2a,b), indicating that deep ventilation may have occurred during the brief 2016 polynya. This modified subsurface water mass persisted into 2017 and was punctuated in October and November by warm and salty intrusions indicative of deep

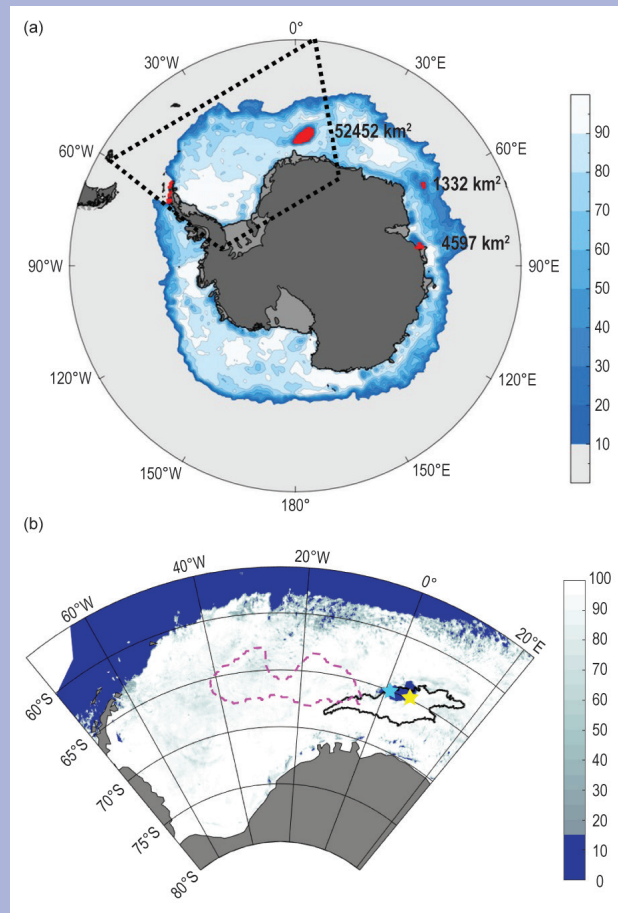


**FIG. SB6.1.** (a) Circumpolar map of AMSR2 sea ice concentration (in %) on 8 Nov 2017, with the red shading marking polynya locations, including the largest—the Maud Rise polynya. (b) Location of the polynya on 14 Oct 2017 from AMSR2 sea ice concentration (Spren et al. 2008). The black line represents the polynya size on 29 Nov 2017, at its largest extent just prior to coalescing with the open ocean. The yellow and cyan stars represent the location of the SOCCOM floats 5904471 and 5904468, respectively. The magenta contour shows a 20-yr mean location of the polynya as depicted in the MPI-ESM-LR model.

mixing during the 2017 polynya event. Additionally, enhanced biogeochemical responses to the polynya’s presence were observed with approximately a 2-month earlier (September 2017) increase in chlorophyll fluorescence (phytoplankton) and pH (Figs. SB6.2c,d) compared to the two previous years, which were ice covered. Hydrographic measurements collected near Maud Rise during two research expeditions on the R/V S.A.

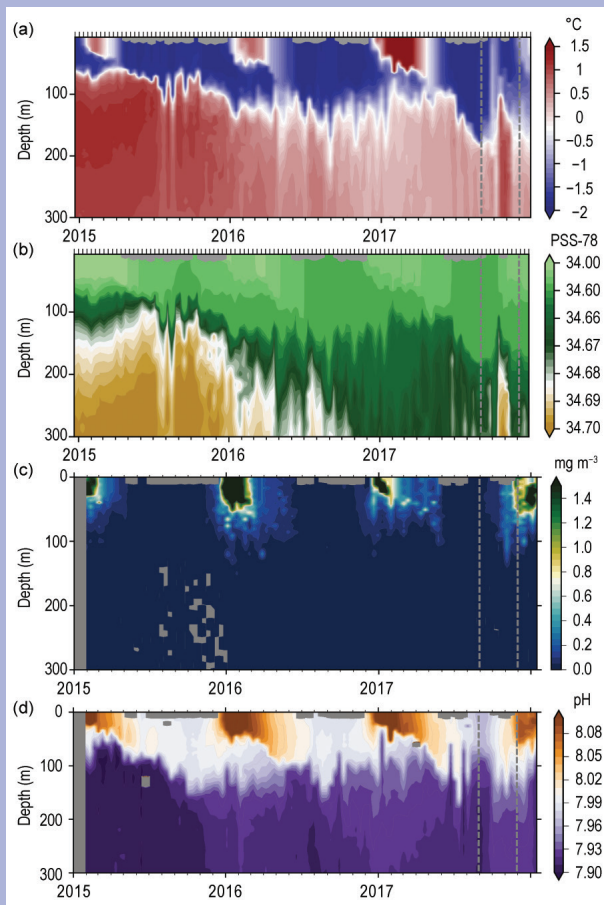


**FIG. SB6.2.** Sections of (a) potential temperature ( $^{\circ}\text{C}$ ), (b) salinity (PSS-78) from SOCCOM float 5904471, (c) chlorophyll- $a$  ( $\text{mg m}^{-3}$ ), and (d) pH from SOCCOM float 5904468, from within the polynya over 3 years. Gray dashed lines represent the start and end dates of the 2017 polynya. Gray shading indicates absence of data.

*Agulhas II* and *R/V Polarstern* in December 2017 and January 2018, respectively, when fully processed and analyzed, may lend additional insights regarding the ocean impacts from the 2016 and 2017 polynyas.

The research community continues to speculate on the causes of the 2017 polynya and whether it is related to the 2016 event. It is possible that the 2017 polynya was caused by persistent subsurface ocean conditions that were initiated during the 2016 polynya, and/or it was caused by preconditioning that resulted from anomalous sea ice divergence occurring late spring 2016 (Schlosser et al. 2018). Preconditioning mechanisms may include a build-up of subsurface heat (Martin et al. 2013), a precipitation deficit caused by prolonged negative

SAM (Gordon et al. 2007), and/or reduced sea ice concentration and upper-ocean instability from upwelling of warm and salty waters on the flanks of Maud Rise (Gordon and Huber 1995; Lindsay et al. 2004; de Steur et al. 2007; Cheon et al. 2014, 2015). Triggering mechanisms remain less clear but may include transient eddies or other topography–mean flow interactions associated with Maud Rise (Holland 2001) or small positive salinity anomalies at the surface caused by anomalous wind and/or sea ice conditions (Cheon et al. 2014; Heuzé et al. 2015; Kjellsson et al. 2015). A prolonged period of strong westerly winds (coincident with positive SAM) might also explain the 2016 and 2017 openings that may have responded to the wind-induced Ekman transport and associated upwelling of warmer water (Cheon et al. 2014; Ferreira et al. 2015). In the lead-up to the 2016 and 2017 polynyas, the SAM index was indeed strongly positive with three of its ten highest monthly values since 1957 recorded in 2015 and 2016, including the largest value in February 2015—coinciding with the annual sea ice minimum. It is quite possible that strong winds and an associated enhanced Weddell Gyre were the catalyst for these polynya events. A contributing mechanism during both years may be anomalously warm waters advecting south from the Indian and western Atlantic sectors of the Southern Ocean. More research is needed to better understand the respective roles of large-scale modes (SAM) versus regional circulation anomalies, in addition to needing more highly resolved data in space and time (e.g., Schlosser et al. 2018).

Global coupled models generally exhibit a greater frequency of Maud Rise polynya occurrence compared to observations (e.g., Heuzé et al. 2013; Fig. SB6.1b) and have thus been a valuable source of information regarding their causes and occurrences. Models suggest a preconditioning is needed by the slow accumulation of subsurface heat over several decades (Martin et al. 2013; Dufour et al. 2017), heat that would be lost after years of the polynya remaining open, possibly explaining why polynyas on the scale of the 1974–76 event have not been seen in 40 years. Alternatively, models also suggest that increased freshening at the ocean surface, caused by increased ice sheet/iceberg melt for example, may increase stratification and reduce the frequency of polynya formation (Kjellsson et al. 2015). The extent to which such models robustly reproduce the real ocean is largely unknown due to the comparatively short observational record, but such results highlight the need to better understand this intermittent but important mode of deep ocean ventilation.

float observations in the upper 30 m at intervals of 5 days, 5-m depth, 3° latitude, and 10° longitude of the GLODAPv2 1992–2013 observations (Fig. 6.10f, red and blue pluses for 2017 and 2014–16 float data comparisons, respectively).

The two estimates reveal consistent trends (determined by least-squares fit) in pH, hence ocean acidification. The first approach resulted in an acidification rate of  $-0.0023 \text{ yr}^{-1}$ ; for the second method the rate was  $-0.0025 \text{ yr}^{-1}$  and  $-0.0028 \text{ yr}^{-1}$  for the 2014–16 and 2017 float data comparisons, respectively, implying either the 2017 floats sampled lower pH (than was sampled in 2014 to 2016) or the 2017 floats captured different spatial variability. These results are nevertheless consistent with previous observations based on individual hydrographic lines (Rios et al. 2015; Williams et al. 2015) or based on predictions from coupled models. Faster acidification rates in the Southern Ocean compared to the global average ( $\sim -0.0017 \text{ year}^{-1}$ ) expected due to low carbonate ion concentrations in the Southern Ocean (McNeil and Matear 2008; Orr et al. 2005). Nonetheless, there is considerable spatial and temporal variability in surface ocean pH, both in observed and as predicted with coupled climate models (Russell et al. 2018), but as the float record expands and lengthens, both the assessment and prediction of the spatial and temporal variability in acidification rates will improve.

**g. 2017 Antarctic ozone hole**—N. Kramarova, P. A. Newman, E. R. Nash, S. E. Strahan, C. S. Long, B. Johnson, M. L. Santee, I. Petropavlovskikh, G. O. Braathen, and L. Coy

Severe ozone depletion in the Antarctic stratosphere has been observed every austral spring since the early 1980s (WMO 2014) and is caused by heterogeneous chemical reactions with human-made chlorine- and bromine-containing compounds. As much as 98% of the ozone in the lower stratosphere around 70 hPa is destroyed in September–October. As a result of regulations set in place by the Montreal Protocol and its amendments, levels of chlorine from ozone depleting substances have gradually declined, and springtime Antarctic ozone is beginning to show signs of recovery (WMO 2014).

The 2017 Antarctic ozone hole was the second smallest since 1988, with an area of 17.4 million  $\text{km}^2$  (or 6.7 million  $\text{mi}^2$ ) averaged from 7 September to 13 October, the period of greatest ozone depletion. The ozone hole area is defined as the area with total column ozone values less than 220 Dobson units (DU). Figure 6.11d displays the daily areal coverage of the ozone hole for 2017 (black curve). The area started expanding at the beginning of August, with

a dip due to stratospheric warming in mid-August. It increased until another stratospheric warming stopped the expansion in mid-September, reaching a 19.6 million  $\text{km}^2$  peak on 11 September, and then declined slowly into October and disappeared on 19 November. The warmings prevented the hole from

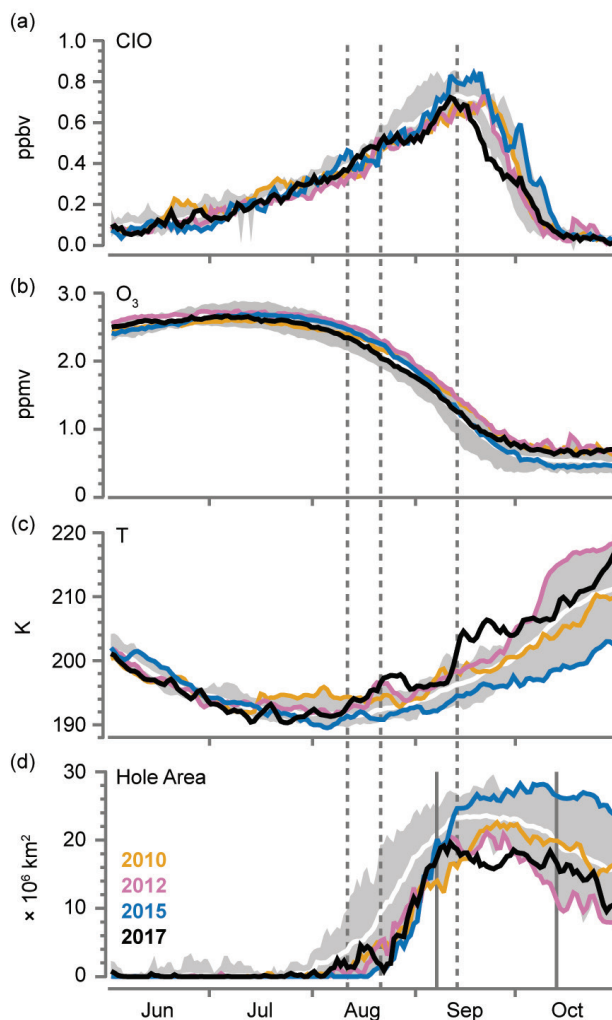


**FIG. 6.11.** Antarctic vortex-averaged concentrations of: (a) ClO and (b) ozone from *Aura* MLS (updated from Manney et al. 2011). These MLS averages are made inside the polar vortex on the 440-K isentropic surface ( $\sim 18 \text{ km}$  or 65 hPa). (c) Temperature on the 440-K isentropic surface over Antarctica ( $60^\circ\text{--}90^\circ\text{S}$ ) from MERRA-2 (Gelaro et al. 2017). (d) Ozone hole area based on Ozone Monitoring Instrument (OMI) and Ozone Mapping and Profiler Suite (OMPS) satellite observations. Four years are shown: 2010 (orange), 2012 (pink), 2015 (blue), and 2017 (black). The white line shows the daily average and the gray shading shows the daily ranges for 2005–16. The vertical solid lines indicate the averaging period for Fig. 6.13, while the vertical dashed lines indicate the dates of maximum wave forcing for the stratospheric warming events in 2017.

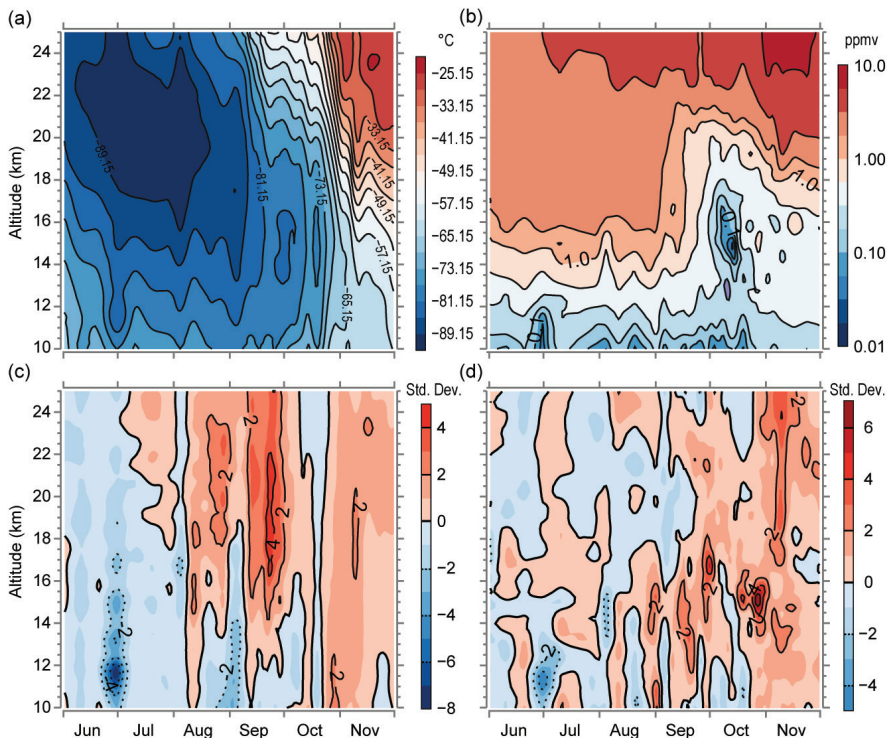


**FIG. 6.12.** Altitude vs. time cross sections from balloon observations at South Pole station in 2017 for: (a) temperature profiles (°C), (b) ozone profiles (ppmv), and anomalies from the 2005–16 average normalized by std. dev. of (c) temperature and (d) ozone.

growing further, accounting for the low average area compared to previous years.

The extent of the seasonal ozone depletion over Antarctica is controlled by the total inorganic chlorine and meteorological conditions in the lower stratosphere. Colder temperatures facilitate formation of the polar stratospheric clouds (PSC) and transformation of inorganic chlorine to active chlorine that eventually lead to ozone loss. There were two key planetary wave events in the lower stratosphere that slowed ozone depletion (and thus the areal expansion of the ozone hole). The first occurred between 11 and 21 August, and the second on 13 September. These disturbed the polar vortex and warmed the lower Antarctic stratosphere (Fig. 6.11c). Satellite observations acquired by the NASA *Aura* Microwave Limb Sounder (MLS) show that ClO (chlorine monoxide) levels rose until the 13 September planetary wave event and then rapidly declined (Fig. 6.11a, black curve), stalling this year's ozone depletion (Fig. 6.11b). The seasonal evolution of the stratospheric ozone concentration, ozone hole area, ClO, and temperature in 2017 is similar to those in 2010 and 2012—two other years with unusually strong wave activity that resulted in higher-than-average stratospheric temperatures and smaller-than-average ozone holes.

In July 2010, a wave event warmed the stratosphere, followed by little wave activity until a mild event early in September of that year. The 2010 ozone hole slowed its areal growth but continued to develop in a normal manner with reduced values. In 2012, the development of the ozone hole proceeded as in 2017, but large wave events happened in late September into October. In contrast to these active years, 2015 was a year with little planetary wave activity and consistently lower-than-average temperatures throughout the austral winter and spring. Consequently, 2015 had severe Antarctic ozone depletion and a larger ozone hole area.

Balloon ozone and temperature observations at South Pole station (Fig. 6.12) revealed the record high temperatures in the stratosphere above ~15 km in August and September, soon after the wave events. These temperatures were 2–4 standard deviations higher than the average seasonal values derived from the balloon observations over the period 2005–16 (Fig. 6.12c). The above-average stratospheric temperatures over the South Pole led to weak ozone depletion this year (Fig. 6.12d). Even though the ozone values dropped below 0.1 ppm in October between 12 and 18 km (Fig. 6.12b), the anomalies show that compared to previous years, ozone concentrations were 3–6 standard deviations above the mean, consistent with smaller ozone loss.

The weaker 2017 ozone depletion has further strengthened the long-term downward trend seen in the annual ozone hole area since the early 2000s (Fig. 6.13). Since 1988, the only ozone hole smaller than the 2017 hole was observed in 2002, when the only major stratospheric warming on record rapidly warmed the polar vortex in late September and drastically limited ozone depletion. The 2017 wave events noted above, while strong, were still smaller in amplitude than those in 2002. Moreover, the 2017 wave events occurred earlier in September, stalling the typical seasonal evolution of ozone depletion. Because of

that, the maximum daily area in 2017 (the top of the vertical gray bars in Fig. 6.13) was the smallest since 1988, at 19.6 million km<sup>2</sup>.

MLS observations for 2004–16 show that inorganic chlorine (Cl<sub>y</sub>) levels in the Antarctic lower stratospheric vortex have declined on average 25 ppt yr<sup>-1</sup>, directly attributable to the Montreal Protocol and its amendments (Strahan et al. 2014; Strahan and Douglass 2017). Year-to-year meteorological variability can cause dynamically driven multiyear Cl<sub>y</sub> increases in the Antarctic, as occurred from 2013 to 2017, in spite of the overall downward trend in stratospheric chlorine loading. Year-to-year Cl<sub>y</sub> variations and large temperature variability in late September and October complicate the attribution of the decline in hole area (Fig. 6.13) to declining chlorine levels. The appearance of a downward areal trend in the last decade is mostly driven by higher spring temperatures in the lower stratosphere. In Fig. 6.13, ozone holes in the last two decades with September Antarctic lower stratospheric temperatures one standard deviation below the average are highlighted in blue. It is apparent that these cold years produce ozone hole areas with similar size and show no clear trend in area. Depletions in recent years are consistent with current knowledge of the photochemical destruction driven by chlorine and bromine compounds and stratospheric temperatures and circulation.

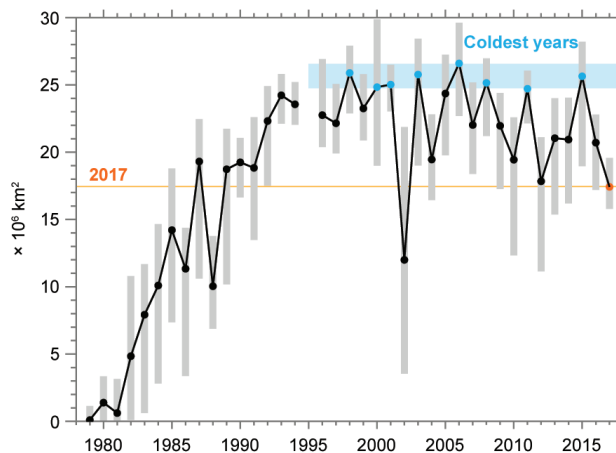


**FIG. 6.13. Average Antarctic ozone hole area calculated between 7 Sep and 13 Oct (dots), along with the range of daily values over this period (gray vertical bars). The value for 2017 is highlighted (orange dot and horizontal line). The years with significantly cold temperatures since 1995 are highlighted (blue dots) and the horizontal blue band indicates the range of the associated ozone hole areas. Data for 1979–92 are from Total Ozone Mapping Spectrometer (TOMS) Nimbus-7; 1993–94 are from TOMS Meteor-3; 1996–2004 are from; 2005–15 are from Aura OMI; and 2015–17 are from Suomi National Polar-orbiting Partnership (SNPP) Ozone Mapping and Profiler Suite (OMPS). There were no satellite total ozone observations for 1995.**